

Design and Evaluation of a Needle Manipulation System with EM Tracking for CT-Guided Spinal Injections

Chang Chang¹, Junling Mei², Yanzhou Wang¹, Lidia Al-Zogbi¹, Simon Leonard³, Amit Jain⁴, and Iulian Iordachita¹

Abstract—This paper presents a flexible needle guidance system and its workflow that enables registration of computed tomography (CT) and electromagnetic (EM) tracking systems with a finite element (FE) simulator for needle-based percutaneous spinal injections. CT is used only pre- and postoperatively for surgical planning and confirmation, while EM tracking is combined intraoperatively with an FE-based needle controller to track the planned needle trajectory and avoid obstacles. Evaluation of the proposed system using a multi-layer soft tissue phantom shows an average targeting accuracy of 0.4mm.

I. INTRODUCTION

Low back pain (LBP) is a prevalent musculoskeletal issue that impacts millions globally, ranking as a major cause of disability in terms of years lived with disability [1]–[3]. In addition to common causes like injuries sprains, and strains, other factors such as age, pregnancy, and weight gain can also contribute to the development of LBP [4].

Spinal injections are minimally invasive, needle-based procedures performed percutaneously to both diagnose and alleviate LBP, often used in conjunction with diagnostic imaging [5], [6]. For instance, during a lumbar facet joint injection, the patient is positioned prone on the scanner table while the physician inserts a spinal needle into the targeted area, using either CT [7]–[10], magnetic resonance imaging (MRI) [11]–[13], fluoroscopy imaging [14], [15] and ultrasound [16]–[18] for real-time guidance. Once the needle is correctly positioned, medication is injected.

Despite the significant improvements in needle placement accuracy with intraoperative imaging, the frequent use of X-rays exposes both patients and physicians to ionizing radiation, increasing their risk of cancer and potentially limiting treatment access for vulnerable populations [19]–[23]. It is, therefore, paramount to reduce radiation exposure while ensuring the accuracy of insertion during the procedure, and recent advances in medical robotic systems and control

This work is supported by NIH R01EB020667, R01EB036015, R01CA235134, and in part by a collaborative research agreement with the Multi-Scale Medical Robotics Center in Hong Kong.

¹Chang Chang, Lidia Al-Zogbi, Yanzhou Wang, and Iulian Iordachita are with the Department of Mechanical Engineering and the Laboratory of Computational Sensing and Robotics, Johns Hopkins University, Baltimore, MD, USA. ywang521@jh.edu

²Junling Mei is with the Laboratory of Computational Sensing and Robotics, Johns Hopkins University, Baltimore, MD, USA.

³Simon Leonard is with the Department of Computer Science and the Laboratory of Computational Sensing and Robotics, Johns Hopkins University, Baltimore, MD, USA.

⁴Amit Jain is with the Department of Orthopaedic Surgery, Johns Hopkins University School of Medicine, Baltimore, MD, USA.

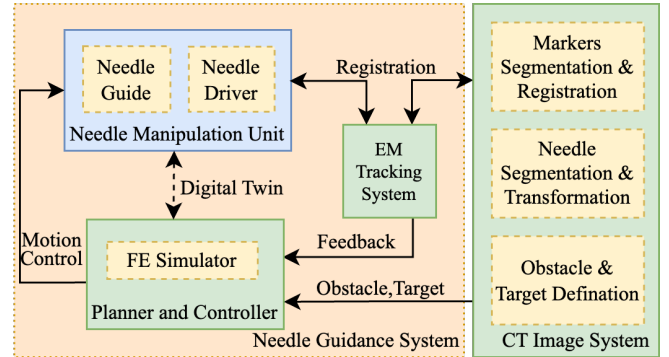


Fig. 1: Needle manipulation system diagram. Green blocks represent software and the blue blocks represent hardware.

methods are reducing the reliance on high-risk imaging modalities. For example, Adagolodjo *et al.* [24] presented an integrated system to perform fully robotic needle insertions into a deformable foam. By tracking optical markers attached on the foam and updating their finite element simulation, the system is able to follow an arbitrary needle path with an average error along the trajectory of 1.62 mm with a maximum error of 3.73 mm. Kuntz *et al.* [25] developed a medical robot that autonomously navigates a highly flexible needle under EM tracking for lung biopsies. In live animal studies, the authors report a targeting error of less than 5mm, around 40mm insertion depths. Squires *et al.* [26] proposed an MRI-guided needle positioning system using a buffer controller. It has a mean accuracy of 2.2 mm and a standard deviation of 0.85 mm in a swine cadaver test. Chen *et al.*'s ultrasound-guided needle insertion system could reach a mean error of 0.9 mm with a standard deviation of 0.29 mm [27].

This paper builds on our previous work on FE-based flexible needle manipulation for needle insertion control and presents an integrated system for CT-guided spinal injections with EM tracking. The rest of this paper is as follows: Section II-B introduces the system's architecture and communication. Section II-C and Section II-D show the system's hardware design and fabrication. Section II-E and Section II-F describe the planner and tracker based on FE simulated as well as EM tracking system integration. Section III explains the integration of CT image system, including marker segmentation, registration, needle segmentation and fitting, and the target and obstacle definition. Section II-A explains

the entire workflow for our system. Section IV, Section V, and Section VI present the experimental setup, results and discussion, conclusion and future work, respectively.

II. NEEDLE GUIDANCE SYSTEM

A. System Workflow

Our system workflow is summarized as follows. After positioning the robot with limit switches, the EM system is registered to the FE simulator as detailed in Section III-A. During this registration process, the needle manipulation unit must be kept from the CT scanner at least 1 meter away to minimize interference with the EM tracking system. The methods of integrating tracking information and evaluating EM disturbance are elaborated in Section II-E and [28].

Subsequently, the "patient" (phantom) and EM tracking system are positioned under the CT scanner for a preoperative scan, followed by these steps:

- 1) Segment the CT images and register them with the EM tracking system, as described in Section III-B.
- 2) Segment and fit the needle, as outlined Section III-C.
- 3) Define target and outline obstacles using the method described in Section III-D.

After defining the target and obstacles, the planner iteratively optimizes the plan to identify a minimally invasive insertion strategy. This plan aims to accurately place the needle tip at the target while navigating around obstacles and minimizing excessive tissue compression. Once an optimal plan is generated, the tracker executes a hybrid model predictive controller with a bang-bang controller to track the planned trajectory, utilizing a tip sensor as feedback.

Finally, the setup is repositioned under the CT scanner for a postoperative confirmation scan to evaluate the actual targeting accuracy.

B. System Architecture and Communication

As shown in Figure 1, the needle guidance system comprises three main components: the needle manipulation unit, the planner and tracker, and the EM tracking system.

All the motors within the needle manipulation unit are independently controlled by a motion controller (DMC-4143, Galil Motion Control, USA). The channels controlling the motor responsible for needle translation and the motor for guide motion are configured as contour mode, enabling simultaneous needle insertion and guide motion. Needle rotation is performed before insertion and guides motion in every single step, preventing the needle from deviating from its predefined plane. The motion controller communicates with two ROS2 nodes over Ethernet. One of the nodes serves as a ROS2 server, which uses gclib (Version 2.0.8, Galil Motion Control, USA) to send commands to the controller based on MATLAB requests. The second node acts as a publisher, broadcasting all encoder positions at 40Hz as feedback to the planner and tracker.

An offline trajectory planner and an online tracker with EM feedback control the needle manipulation unit [28]. For each target defined by CT image system, the planner generates a path prior to moving the unit. Subsequently, the

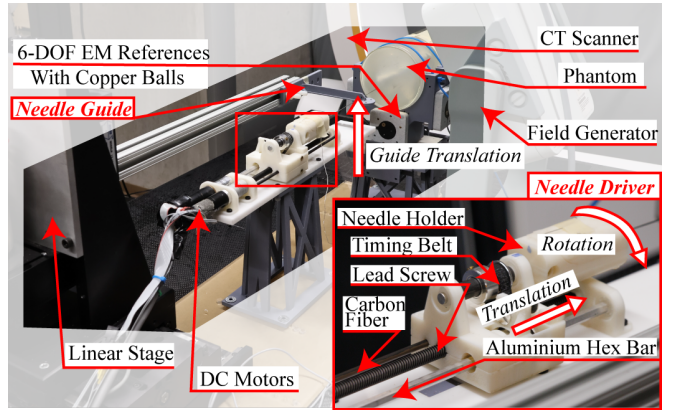


Fig. 2: Experimental setup for needle insertion experiments using a soft tissue phantom.

real-time tracker manipulates the needle according to the planned trajectory via ROS2.

All EM references and the needle tip sensor (Aurora, Northern Digital, Canada) are connected to a ROS2 publisher by a USB port. Additionally, a tf2 node processes the transformation data published by the publisher.

C. Needle Driver Design and Fabrication

As illustrated in Figure 2, the 2-DOF needle driver within the needle manipulation unit translates and rotates the needle, powered by two identical RE16 motors (Maxon Group, Switzerland) with three limit switches (ESE-22MH54, Panasonic Electronic Components, Japan). To minimize moving mass and EM interference, the needle is not directly rotated by the motor. Instead, a timing belt mechanism rotates the needle via an aluminum hex bar, while the second motor translates the needle using a lead screw and nut mechanism. This configuration positions motors as far from the workspace and the EM tracking system as possible. The needle driver provides 110mm of axial translation and continuous rotation. However, the needle's rotation is fixed at 0° and 180° in our experiments.

D. Movable Needle Guide and Linear Stage

A movable needle guide is actuated by a vertical linear stage (Dover Motion, USA). A long aluminum profile allows the linear stage to be situated far back beyond the field generator region so as to eliminate interference introduced by the linear stage to EM field. A long guide is used to make the aluminum profile as far as possible from the sensor in the needle and the field generator, reducing the interference caused by the aluminum profile as in [29].

E. EM Tracking System Integration

There are three 6-DOF EM references mounted on the tissue phantom, namely reference 0, reference 1, and reference 2. Figure 3 shows locations of all references. One 5-DOF reference is embedded in the needle tip to track its position and orientation except for rotation around the needle. All references are covered by an electromagnetic field created

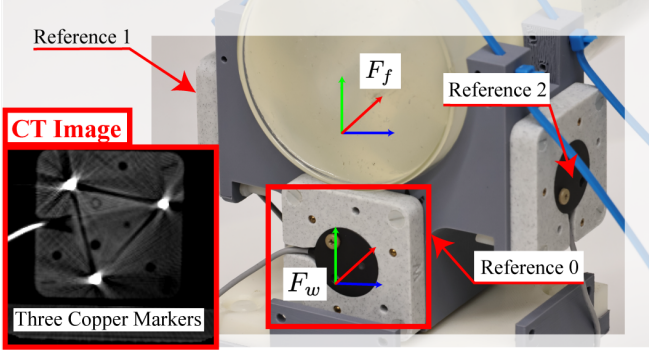


Fig. 3: Location of all frames and how they appear in CT.

by a generator and their orientations and positions w.r.t. the generator frame would be logged by a ROS2 node and published in ROS2 net in real-time. These transformations are subscribed by another node and construct a ROS2 tf tree. The needle tip is also added to the tree. The frame F_w attached on 'reference 0' is used as the base frame for the EM tracking system, which means other references' data are processed w.r.t. F_w retrieved from ROS2. To offer real-time feedback to FE simulator, a registration process is needed and explained in Section III-A.

F. Needle Planner and Controller

Our planning and tracking framework is based on iterative trajectory sampling within a FE simulator. The simulator assumes an inextensible beam model for the flexible needle and one-term Ogden-type hyperelastic material for soft tissues [30]. The simulator updates the discretized needle states vector X actuated by control inputs U with running the real-time FE simulation forward in time. Three needle control inputs considered in current work – translation, rotation, and lateral guide motion – can be obtained iteratively through the cross-entropy method by sampling from the simulator and reducing the cost associated with each sampled trajectory [28].

High targeting accuracy, low tissue damage, and obstacle avoidance are desirable objectives for a needle insertion task. Therefore, the cost J associated with each planned insertion can be written as

$$J(X, U) = J_f(X_f) + \sum_s J_s(X_s, U_s), \quad (1)$$

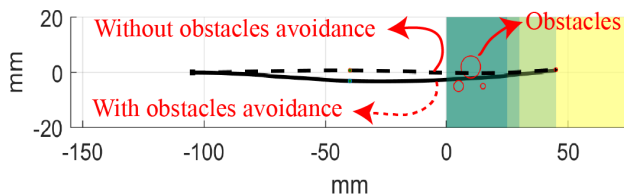


Fig. 4: Different paths generated by the planner in F_f . The solid line and the dashed line are the needle manipulated with/without obstacle avoidance.

where J_f is the final cost that includes targeting error and total tissue compression, which can be recovered by the final needle state X_f and the simulator; step cost J_s includes penalties to "risky" needle maneuvers that might cause tissue damage, such as large needle guide translation and excessive needle axial rotations. (X_s, U_s) denotes the state and input in one step. In addition to penalty terms considered in [28], we include additional costs for the needle being too close to or penetrating forbidden regions. We call these forbidden regions "obstacles", which are integrated into the cost J_{obs} as

$$J_{\text{obs}} = \alpha J_{\text{in}} + \beta J_{\text{dist}}, \quad (2)$$

where α, β are parameters to balance the impact from different penalties. J_{in} is to detect if the needle's points are on or in the obstacles' boundary.

$$J_{\text{in}} = \sum_{n=1}^{N_{\text{nodes}}} \sum_{m=1}^M \mathbb{1}(\mathbf{x}_n \in \mathcal{O}_m), \quad (3)$$

where \mathcal{O}_m is a set of obstacles, M is the number of points in \mathcal{O}_m and N_{nodes} is the number of nodes in X , \mathbf{x}_n is a point in X , $\mathbb{1}(\cdot)$ is the indicator function, which equals 1 if the condition is true, and 0 otherwise. J_{dist} is a proximity-based penalty item.

$$J_{\text{dist}} = \sum_{n=1}^{N_{\text{nodes}}} \sum_{m=1}^M \max(0, d_{\text{thresh}} - d(\mathbf{x}_n, \mathcal{O}_m)). \quad (4)$$

d_{thresh} is a distance threshold, excluding points that have a distance larger than the threshold. $d(\mathbf{x}_n, \mathcal{O}_m)$ represents the minimum Euclidean distance from the point \mathbf{x}_n to the obstacle \mathcal{O}_m .

$$d(\mathbf{x}_n, \mathcal{O}_m) = \min_{\mathbf{o}_m^{(i)} \in \mathcal{O}_m} \|\mathbf{x}_n - \mathbf{o}_m^{(i)}\|, \quad (5)$$

where $\mathbf{o}_m^{(i)}$ is one obstacle in \mathcal{O}_m .

Figure 4 shows the different paths that the planner generates in the same scenario. The solid line is the path with the obstacle avoidance penalty J_{obs} . It avoids the obstacles we defined instead of penetrating them like the dashed line path. Once an optimal trajectory has been generated, the tracker then follows the nominal trajectory while taking needle tip EM reading as feedback [28].

III. CT IMAGE PROCESSING AND REGISTRATION

All CT scans are collected by using a cone-beam CT machine (Loop-X, BrainLab, Germany) whose smallest voxel size is $0.46 \times 0.46 \times 0.46 \text{ mm}^3$. In order to define the target prior to the procedure and ascertain if the needle tips reached the target point after insertion, two CT scans are produced during the whole workflow. A preoperative scan is performed during initialization, i.e. the needle tip is on the skin surface but has not yet been inserted. In this step, the target point and any obstacles are selected. After the entire insertion process, a postoperative scan is performed to evaluate the result of insertion.

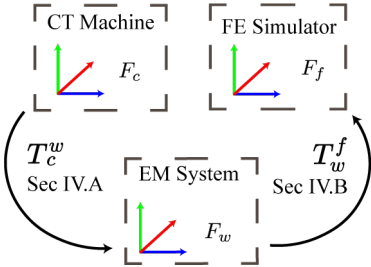


Fig. 5: Three main frames in the overall system and their transformations. F_f stands for the FE simulator, F_c for CT image frame, and F_w connects F_f and F_c .

As shown in Figure 5, the entire system mainly has three frames F_w , F_f , and $F_c \in SE(3)$. F_w is attached to the reference 0 shown in Figure 3. F_f represents the coordinate system used by the FE simulator, with its origin precisely located at the point where the needle penetrates the surface of the phantom. F_c contains all CT images.

A. Registration to FE Simulator

To convert needle tip's coordinates w.r.t. F_w into F_f , a registration is performed to determine the transformation T_w^f from F_w to F_f . Initially, the robot calibrates itself with the help of limit switches. Then the needle tip is moved to a suitable position. The first two positions located 3mm and 8mm away from the origin of the F_f (See Figure 3) should be as close as possible to the center of the EM field, and the needle manipulation unit should not touch anything when moving, which would cause unexpected needle bending. The third position is right on the origin of the F_f . Each position has 50 samples and the mean values of these measurements are used as \vec{p}_1^w , \vec{p}_2^w , \vec{p}_0^w w.r.t. the frame F_w . At \vec{p}_2^w , we move the guide vertically up and record \vec{p}_3^w using the same method as in the previous step. This time we pick 5mm according to the previous consideration. Three vectors could be derived by

$$\vec{x}^w = \frac{\vec{p}_2^w - \vec{p}_1^w}{\|\vec{p}_2^w - \vec{p}_1^w\|}, \quad (6)$$

$$\vec{z}^w = \vec{x}^w \times \frac{\vec{p}_3^w - \vec{p}_2^w}{\|\vec{p}_3^w - \vec{p}_2^w\|}, \quad (7)$$

$$\vec{y}^w = \vec{x}^w \times \vec{z}^w, \quad (8)$$

With these vectors, the transformation $T_w^f \in SE(3)$ from F_w to F_f is constructed by

$$T_w^f = \begin{bmatrix} \vec{x}^w & \vec{y}^w & \vec{z}^w & \vec{p}_0^w \\ 0 & 0 & 0 & 1 \end{bmatrix}^{-1}. \quad (9)$$

B. Marker Segmentation and Registration

Figure 6 shows the overall workflow. To register the EM tracking system with the CT image, three sets of 3mm diameter copper markers are embedded in three 3D-printed parts, each associated with an EM reference as shown in Figure 3. Each set contains 6 markers, whose coordinates w.r.t. the nearest EM reference are obtained from the Solidworks 2024

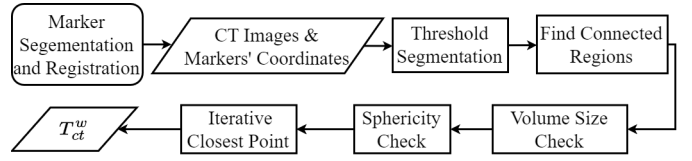


Fig. 6: Marker segmentation and registration workflow.

(Dassault Systems, Franch). As shown in Figure 3, copper markers appear as nearly spherical clusters with intensities higher than any other objects in CT images, as the phantom and needle driver contain minimal metal components detectable in CT. A threshold segmentation is performed to identify connected regions, eliminating unexpected items such as noise by checking their volume size. To isolate the copper markers, a sphericity check filters out regions that do not match the shape of a sphere. The centers of segmented spheres are then used as their coordinates w.r.t. F_c . Finally, an iterative closest point (ICP) algorithm is executed to compute the transformation T_c^w from F_c to F_w using copper markers coordinates w.r.t. both frames. As detailed in Figure 7, all the copper markers in F_w align with their counterparts in F_c .

C. Flexible Needle Segmentation and Fitting

1) *Needle Segmentation*: Figure 8 presents a flowchart of needle processing. Similar to markers segmentation, it begins with threshold segmentation. However, a lower threshold is used for the needle due to its thinner diameter which results in a lower intensity than the copper balls. This low threshold helps preserve the needle's details, preventing it from fragmenting the needle into multiple segments. The resulting 3D intensity image is converted into a set of point clouds by identifying connected regions. There are still some unexpected point clouds such as the bone model in this set due to the low threshold. To remove these, we examine the size of all the point clouds and eliminate those exceeding a

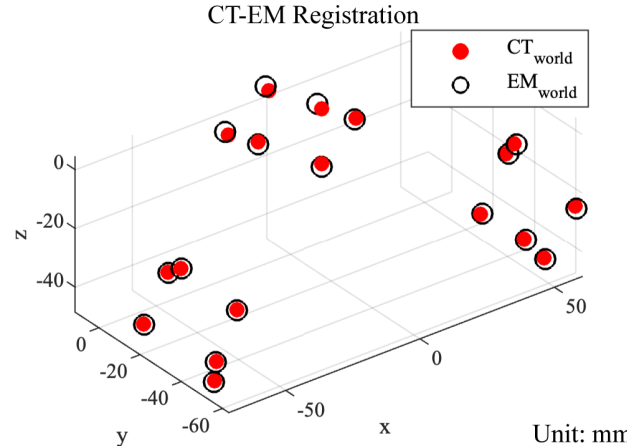


Fig. 7: Registration results. The red solid dots are copper markers in F_w transformed from F_c and the black circles are copper balls in F_w .

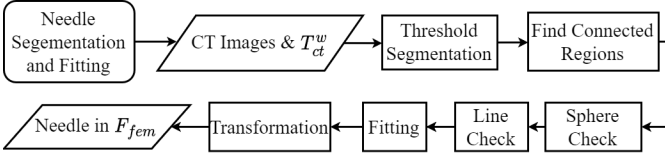


Fig. 8: Needle segmentation and fitting workflow.

specified point count. After removing large point clouds, the binary image is converted into coordinates with a scale factor extracted from the metadata of CT scans. A line check is then conducted using a 5mm sphere centered at the centroid of every point cloud. A ratio r_{line} is given by

$$r_{line} = \frac{N_{in}}{N_{all}}, \quad (10)$$

where N_{in} denotes the number of points within the sphere, and N_{all} is the total number of points in the cloud. The 5mm sphere can filter out all the markers and most of the points clusters whose r_{line} is almost 1. We purge all the point cloud whose r_{line} is greater than a threshold. After observations and tests, we determined that 0.4 is an appropriate ratio for our usage, meaning 60% points of itself are in the 5mm sphere and it cannot be a line we need. Following this, only linear structures remain, though some curved wires persist. To isolate the needle, a principle component analysis offers a main direction vector of the points, indicating the possible direction of the needle (see Figure 9). Starting from the first point in the set and extending along the given direction vector, a line in space is defined. Distances from all points in the set to this line are then calculated, and the standard deviation of these distances is determined. The points set with minimum standard deviation is identified as the needle.

2) *Needle Fitting*: The main direction vector obtained in the segmentation process is used as the needle's principal axis in the fitting process. The needle is segmented into 1mm thick slices along the main direction vector, and centroids of slices are treated as data points for the fitted line. The number of slices, N , is determined dynamically. However, the length of the slice N is partially ignored, as it might not reach 1 mm due to an insufficient number of points. As illustrated in Figure 9, a slice compensation is applied. First, the centroids of the slice N and $N - 1$ are connected to determine the center direction. Then, all the points in the slice N are projected along this direction. The slice compensation is derived based on the largest positive distance and the center direction.

The needle tip often disappears in segmentation results, because it becomes smaller in volume, which reduces its intensity or causes it to fall below the resolution of the CT. To address this, a tip compensation collinear with the slice compensation is constructed. The length of it is derived as

$$L_c = \sqrt{L_b^2 - D^2} = \sqrt{1.7^2 - 0.8} \approx 1.5 \text{ mm}, \quad (11)$$

where L_b and D are the length of the needle's bevel and diameter measured by a caliper (Mitutoyo, Japan).

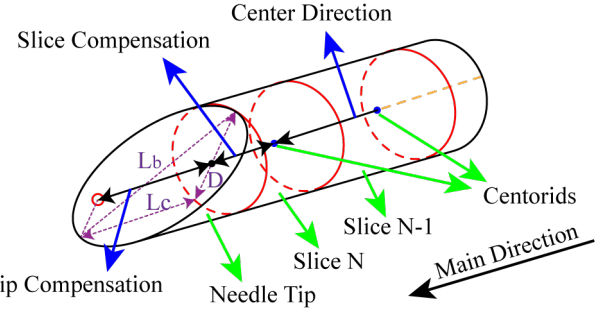


Fig. 9: Compensations in needle fitting. Slice $N - 1$ is 1mm long but Slice N is shorter than 1mm.

D. Target Selection and Obstacle Definition

Before selecting the target and defining obstacles, we should have a CT scan with the needle tip placed at the origin of F_f . To pick targets from the CT image, the image volume from the CT machine is rotated and sliced to align with the F_f so that we can directly pick pixels in the CT image. Picked pixels are rescaled to coordinates in the F_f . With this basic process, we could define the insertion target and the obstacles. As Figure 10a shows, the yellow cross is the target and the blue circles are obstacles. After the insertion process, the post-operation scan is also rotated to the same orientation. The target and obstacles we selected manually in the pre-operation image are transformed into the post-operation image to check the result. Figure 10b shows the final post-operation image.

IV. PHANTOM EXPERIMENT

Phantom experiments are conducted by using the setup shown in Figure 2. The phantom had two layers with different stiffness and a model bone was embedded in the deeper layer [28], [31]. Two sets of experiments were conducted. In the first experiment, we aim to evaluate insertion error using 7 targets selected in the phantom. These targets had a mean depth of 37.6mm and a mean lateral offset is -0.3mm. The

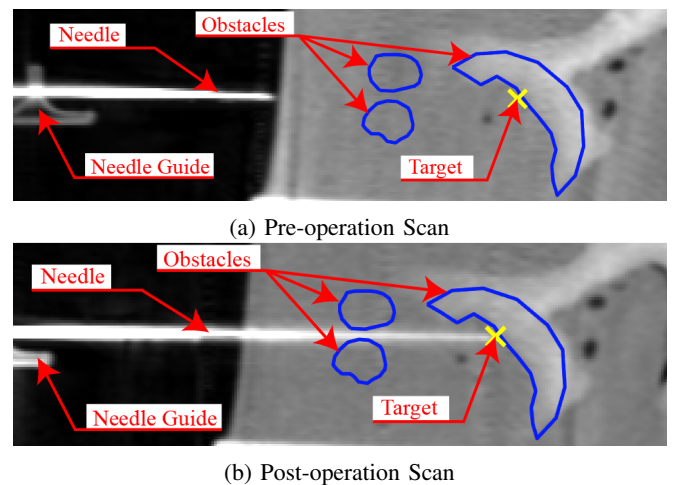


Fig. 10: Preoperative and postoperative CT images.

depth was chosen as it aligns with typical distances in clinical practice [32], [33]. Due to the limited bending capacity of the needle, there is a constrained region around this depth that the needle can theoretically reach. The selection of seven test targets was sufficient to cover this area. In the second experiment, we aimed to verify the performance of our obstacle avoidance algorithm. To simulate the injection scenario, a narrow structure was defined to evaluate whether the algorithm functions as intended.

V. RESULTS AND DISCUSSION

In the first set of experiments, all the targets and results are listed in Table I. The first column shows the targets defined in the CT image. ICP error indicates the registration error when deriving T_{ct}^w , which is defined by

$$ER = \sqrt{\frac{1}{W} \sum_{i=1}^W \|\vec{p}_i - \vec{q}_i\|^2}, \quad (12)$$

where \vec{q}_i represent points in the source frame. \vec{p}_i are points in the target frame transformed into the source frame, and W denotes the number of points in each point cloud. The second column contains distances between the final tip position reported by the EM tracking system and segmented from the CT image. EM errors are differences between targets and the EM tracking system's feedback. The targeting column shows errors between targets and needle tips from segmentation.

According to results in Table I, the ICP process was stable and reliable, as it exhibits a variance close to zero. Although it introduced a small degree of error in the registration process, no significant interference was observed throughout the procedure. Both EM result and targeting results had a mean error less than 0.5mm, with no identified correlation between targeting errors and CT-EM position differences. Notably, an outlier bolded in Table I showed an EM error of 0.39mm but 0.89mm between EM and CT results, along with a targeting error of 1.24mm. One possible reason was that a portion of the needle tip was out of the segmentation plane, likely caused by damage from previous experiments. Such damage may affect the needle trajectory.

Figure 10 illustrates the result of the second experiment. The needle correctly avoided the obstacles we defined and reached the target with a targeting error 0.63 mm.

TABLE I: Test Errors

Unit: mm. All targets and error are measured in F_f				
Target (x, y)	ICP Error	CT to EM	EM	Targeting
42.08, 01.82	1.02	0.89	0.39	1.24
33.92, -02.58	1.01	0.07	0.41	0.47
32.22, 04.33	1.01	0.46	0.28	0.37
33.13, -03.66	1.02	0.16	0.43	0.29
43.73, -00.25	1.02	0.24	0.27	0.10
36.92, 00.12	1.01	0.24	0.14	0.11
35.78, 02.39	1.02	0.27	0.43	0.41
42.97, -04.79	1.01	0.15	0.37	0.24
Variance	0.00	0.06	0.01	0.12
Mean	1.02	0.31	0.34	0.40

VI. CONCLUSION AND FUTURE WORK

In this work, we have successfully built an FE-based flexible needle manipulation system for needle insertion control and presented an integrated system for CT-guided spinal injections with EM tracking. Phantom experiments demonstrated its targeting accuracy is 0.4mm, and it is capable of avoiding obstacles. Future research will focus on real tissue experiments, machine learning-based, more real-time, computationally efficient control methods, and a more integrated system workflow.

REFERENCES

- [1] A. Wu, L. March, X. Zheng, J. Huang, X. Wang, J. Zhao, F. M. Blyth, E. Smith, R. Buchbinder, and D. Hoy, "Global low back pain prevalence and years lived with disability from 1990 to 2017: estimates from the global burden of disease study 2017," *Annals of translational medicine*, vol. 8, no. 6, 2020.
- [2] R. Froud, S. Patterson, S. Eldridge, C. Seale, T. Pincus, D. Rajendran, C. Fossum, and M. Underwood, "A systematic review and meta-synthesis of the impact of low back pain on people's lives," *BMJ musculoskeletal disorders*, vol. 15, pp. 1–14, 2014.
- [3] D. Hoy, P. Brooks, F. Blyth, and R. Buchbinder, "The epidemiology of low back pain," *Best practice & research Clinical rheumatology*, vol. 24, no. 6, pp. 769–781, 2010.
- [4] M. J. DePalma, J. M. Ketchum, and T. R. Saullo, "Multivariable analyses of the relationships between age, gender, and body mass index and the source of chronic low back pain," *Pain Medicine*, vol. 13, no. 4, pp. 498–506, 2012.
- [5] N. Sehgal, E. E. Dunbar, R. V. Shah, and J. Colson, "Systematic review of diagnostic utility of facet (zygapophysial) joint injections in chronic spinal pain: an update," *Pain physician*, vol. 10, no. 1, p. 213, 2007.
- [6] M. V. Boswell, L. Manchikanti, A. D. Kaye, S. Bakshi, C. G. Gharibo, S. Gupta, S. S. Jha, D. E. Nampiaparampil, T. T. Simopoulos, and J. A. Hirsch, "A best-evidence systematic appraisal of the diagnostic accuracy and utility of facet (zygapophysial) joint injections in chronic spinal pain," *Pain physician*, vol. 18 4, pp. E497–533, 2015.
- [7] J. Artner, B. Cakir, H. Reichel, and F. Lattig, "Radiation dose reduction in ct-guided sacroiliac joint injections to levels of pulsed fluoroscopy: a comparative study with technical considerations," *Journal of pain research*, pp. 265–269, 2012.
- [8] B. D. Giordano, J. F. Baumhauer, T. L. Morgan, and G. R. Rechtine, "Cervical spine imaging using standard c-arm fluoroscopy: patient and surgeon exposure to ionizing radiation," *Spine*, vol. 33, no. 18, pp. 1970–1976, 2008.
- [9] F. Costa, G. Dorelli, A. Ortolina, A. Cardia, L. Attuati, M. Tomei, D. Milani, L. Balzarini, F. Galbusera, E. Morenghi, *et al.*, "Computed tomography-based image-guided system in spinal surgery: state of the art through 10 years of experience," *Operative Neurosurgery*, vol. 11, no. 1, pp. 59–68, 2015.
- [10] C. Czerny, K. Eichler, Y. Croissant, B. Schulz, G. Kronreif, R. Schmidt, M. von Roden, C. Schomerus, T. J. Vogl, I. Marzi, *et al.*, "Combining c-arm ct with a new remote operated positioning and guidance system for guidance of minimally invasive spine interventions," *Journal of NeuroInterventional Surgery*, vol. 7, no. 4, pp. 303–308, 2015.
- [11] F. Streitparth, T. Walter, U. Wonneberger, S. Chopra, F. Wichlas, M. Wagner, K. Hermann, B. Hamm, and U. Teichgräber, "Image-guided spinal injection procedures in open high-field mri with vertical field orientation: feasibility and technical features," *European radiology*, vol. 20, pp. 395–403, 2010.
- [12] J. Fritz, P. U-Thainual, T. Ungi, A. J. Flammang, N. B. Cho, G. Fichtinger, I. I. Iordachita, and J. A. Carrino, "Augmented reality visualization with image overlay for mri-guided intervention: accuracy for lumbar spinal procedures with a 1.5-t mri system," *American Journal of Roentgenology*, vol. 198, no. 3, pp. W266–W273, 2012.
- [13] P. J. Grahn, S. J. Goerss, J. L. Lujan, G. W. Mallory, B. A. Kall, A. A. Mendez, J. K. Trevathan, J. P. Felmlee, K. E. Bennet, and K. H. Lee, "Mri-guided stereotactic system for delivery of intraspinal microstimulation," *Spine*, vol. 41, no. 13, pp. E806–E813, 2016.

- [14] P. Merloz, J. Troccaz, H. Vouaillat, C. Vasile, J. Tonetti, A. Eid, and S. Plaweski, "Fluoroscopy-based navigation system in spine surgery," *Proceedings of the Institution of Mechanical Engineers, Part H: Journal of Engineering in Medicine*, vol. 221, no. 7, pp. 813–820, 2007.
- [15] L.-P. Nolte, M. Slomczykowski, U. Berlemann, M. J. Strauss, R. Hofstetter, D. Schlenzka, T. Laine, and T. Lund, "A new approach to computer-aided spine surgery: fluoroscopy-based surgical navigation," *European Spine Journal*, vol. 9, pp. S078–S088, 2000.
- [16] A. Rasoulian, A. Seitel, J. Osborn, S. Sojoudi, S. Nouranian, V. A. Lessoway, R. N. Rohling, and P. Abolmaesumi, "Ultrasound-guided spinal injections: feasibility study of a guidance system," *International journal of computer assisted radiology and surgery*, vol. 10, pp. 1417–1425, 2015.
- [17] S. Chen, Y. Lin, Z. Li, F. Wang, and Q. Cao, "Automatic and accurate needle detection in 2D ultrasound during robot-assisted needle insertion process," *International Journal of Computer Assisted Radiology and Surgery*, vol. 17, no. 2, pp. 295–303, 2022.
- [18] M. Khadem, C. Rossa, N. Usmani, R. S. Sloboda, and M. Tavakoli, "Semi-Automated Needle Steering in Biological Tissue Using an Ultrasound-Based Deflection Predictor," *Annals of Biomedical Engineering*, vol. 45, no. 4, pp. 924–938, 2017.
- [19] N. W. Jenkins, J. M. Parrish, E. D. Sheha, and K. Singh, "Intraoperative risks of radiation exposure for the surgeon and patient," *Annals of Translational Medicine*, vol. 9, no. 1, 2021.
- [20] A. Matityahu, R. K. Duffy, S. Goldhahn, A. Joeris, P. H. Richter, and F. Gebhard, "The great unknown-a systematic literature review about risk associated with intraoperative imaging during orthopaedic surgeries," *Injury*, vol. 48, no. 8, pp. 1727–1734, 2017.
- [21] E. M. Nelson, S. M. Monazzam, K. D. Kim, J. A. Seibert, and E. O. Klineberg, "Intraoperative fluoroscopy, portable x-ray, and ct: patient and operating room personnel radiation exposure in spinal surgery," *The Spine Journal*, vol. 14, no. 12, pp. 2985–2991, 2014.
- [22] D. Mendelsohn, J. Strelzow, N. Dea, N. L. Ford, J. Batke, A. Pennington, K. Yang, T. Ailon, M. Boyd, M. Dvorak, et al., "Patient and surgeon radiation exposure during spinal instrumentation using intraoperative computed tomography-based navigation," *The Spine Journal*, vol. 16, no. 3, pp. 343–354, 2016.
- [23] K. Lee, K. M. Lee, M. S. Park, B. Lee, D. G. Kwon, and C. Y. Chung, "Measurements of surgeons' exposure to ionizing radiation dose during intraoperative use of c-arm fluoroscopy," *Spine*, vol. 37, no. 14, pp. 1240–1244, 2012.
- [24] Y. Adagolodjo, L. Goffin, M. De Mathelin, and H. Courtecuisse, "Robotic insertion of flexible needle in deformable structures using inverse finite-element simulation," *IEEE Transactions on Robotics*, vol. 35, no. 3, pp. 697–708, 2019.
- [25] A. Kuntz, M. Emerson, T. E. Ertop, I. Fried, M. Fu, J. Hoelscher, M. Rox, J. Akulian, E. A. Gillaspie, Y. Z. Lee, F. Maldonado, R. J. Webster, and R. Alterovitz, "Autonomous medical needle steering in vivo," *Science Robotics*, vol. 8, no. 82, p. eadf7614, 2023.
- [26] A. Squires, J. N. Oshinski, N. M. Boulis, and Z. T. H. Tse, "SpinoBot: An MRI-Guided Needle Positioning System for Spinal Cellular Therapeutics," *Annals of Biomedical Engineering*, vol. 46, pp. 475–487, Mar. 2018.
- [27] S. Chen, F. Wang, Y. Lin, Q. Shi, and Y. Wang, "Ultrasound-guided needle insertion robotic system for percutaneous puncture," *International Journal of Computer Assisted Radiology and Surgery*, vol. 16, pp. 475–484, 2021.
- [28] Y. Wang, C. Chang, J. Mei, S. Leonard, and I. Iordachita, "Minimally invasive flexible needle manipulation based on finite element simulation and cross entropy method," *arXiv preprint arXiv:2411.07890*, 2024.
- [29] M. Nakamoto, Y. Sato, Y. Tamaki, H. Nagano, M. Miyamoto, T. Sasama, M. Monden, and S. Tamura, "Magneto-optic hybrid 3-d sensor for surgical navigation," in *Medical Image Computing and Computer-Assisted Intervention-MICCAI 2000: Third International Conference, Pittsburgh, PA, USA, October 11-14, 2000. Proceedings* 3, pp. 839–848, Springer, 2000.
- [30] Y. Wang, L. Al-Zogbi, G. Liu, J. Liu, J. Tokuda, A. Krieger, and I. Iordachita, "Bevel-tip needle deflection modeling, simulation, and validation in multi-layer tissues," in *2024 IEEE International Conference on Robotics and Automation (ICRA)*, pp. 11598–11604, IEEE, 2024.
- [31] Y. Wang, Y. Xu, J. Kang, J. Fritz, and I. Iordachita, "Simulation-based flexible needle control with single-core fbg feedback for spinal injections," *IEEE transactions on medical robotics and bionics*, 2024.
- [32] J. Westbrook, S. Renowden, and L. Carrie, "Study of the anatomy of the extradural region using magnetic resonance imaging," *British Journal of Anaesthesia*, vol. 71, no. 4, pp. 495–498, 1993.
- [33] B. T. Sitzman and D. R. Uncles, "The effects of needle type, gauge, and tip bend on spinal needle deflection," *Anesthesia & Analgesia*, vol. 82, no. 2, pp. 297–301, 1996.